Journal of Materials Research and Technology 30 (2024) 5497–5511

Contents lists available at ScienceDirect

Journal of Materials Research and Technology

journal homepage: www.elsevier.com/locate/jmrt

Crack mitigation strategies for a high-strength Al alloy $Al_{92}Ti_2Fe_2Co_2Ni_2$ fabricated by additive manufacturing

Anyu Shang, Benjamin Stegman, Daniel Sinclair, Xuanyu Sheng, Luke Hoppenrath, Chao Shen, Ke Xu, Emiliano Flores, Haiyan Wang, Nikhilesh Chawla, Xinghang Zhang *

School of Materials Engineering, Purdue University, West Lafayette, IN, 47907, USA

ARTICLE INFO

Handling editor: SN Monteiro

Keywords:
Additive manufacturing
Aluminum alloys
Cracking
Residual stress

ABSTRACT

Laser powder bed fusion is capable of fabricating aluminum (Al) alloy parts with great geometrical flexibility and rapid prototyping for various industries. However, high strength Al alloys generally suffer from solidification cracks due to the steep thermal gradient associated with the laser fusion process. Here, we report several strategies to mitigate the hot crack susceptibility of a high strength $Al_{92}Ti_2Fe_2Co_2Ni_2$ alloy. Routine processing parameter optimization based on varying laser power and scanning speed has to trade off porosity for producing crack-free parts, making it not suitable for load-bearing structural applications. Furthermore, secondary printing parameters, including laser strip length, laser defocus, scanning strategies, etc., improved printability but were insufficient to eliminate all the cracks. Crack morphology and residual stress measurements indicate that the cracks are generated in the solid state driven by large tensile residual stress, instead of solidification cracking or liquation cracking. Thus, an attempt was made to alleviate the residual stress in a controlled manner. By properly introducing a compliant, sacrificial, scaffold support structure to regulate crack propagation, near fully dense, crack-free parts could be successfully printed. The results were further verified by micro computed tomography, showing that cracking could be arrested in the support before propagating through the parts. This method can be readily applied to other alloy systems without modifying the chemistry.

1. Introduction

Laser powder bed fusion (LPBF), also known as selective laser melting (SLM), is an additive manufacturing technique applicable to metallic parts. Aluminum (Al) alloys find wide applications in marine, automotive, and aerospace industries for their low density, high specific strength, excellent corrosion resistance, and high thermal and electrical conductivities. Though LPBF has been widely used to print a variety of Al alloys, many high-strength Al alloys, e.g., AA 6061 [1] and AA 7075 [2], suffer from limited printability. Multiple defects have been identified in the as-printed state, including porosity, hot cracks, anisotropy, and poor surface quality [3]. Among these types of defects, cracks are usually the most serious and detrimental to mechanical properties.

Extensive efforts have been made to develop and commercialize 3D-printable high-strength Al alloys [4–6]. On the one hand, Al–Si alloys with near eutectic compositions, namely AlSi10Mg and Al–12Si are prominent examples of crack-resistant alloy compositions [7]. Their versatility and reliability in printing stem from a low solidification temperature range bounded by solidus and liquidus lines [8]. As a result, it has been found that the optimization of printing parameters is sufficient to diminish or eliminate pores and cracks in near-eutectic Al-Si [9]. Post-heat treatments [10,11] and second phase additions [12,13] could further diminish defects or tune the mechanical performance. However, the overall strengths of these alloys are significantly lower than the high-strength alloys commonly used in structural components.

On the other hand, attempts have been made to modify the chemistry to achieve printability in high-strength Al alloys. Cracking in the non-weldable high-strength Al alloys is typically attributed to two mechanisms: liquation cracking and solidification cracking [14–19]. Solidification cracking refers to intergranular cracking in the fusion zone during the solidification of the weld metal, whereas liquation cracking denotes cracking due to liquated base metal in the partially melted zone [14]. For Al alloys enriched with solutes, like Zn, Cu, Mg, both cracking mechanisms co-exist [2] and could be interfered or mutually triggered [16,20] due to the cyclic thermal history. Among these two mechanisms, solidification cracking seems more prevailing pondering from the crack

* Corresponding author.
E-mail address: xzhang98@purdue.edu (X. Zhang).

https://doi.org/10.1016/j.jmrt.2024.04.191
Received 15 December 2023; Received in revised form 12 April 2024; Accepted 22 April 2024
Available online 24 April 2024

length and fractography. Solidification cracking is associated with the existence of inter-granular liquid films [16,21,22]. As solidification initiates and progresses, solute atoms in Al alloys are continuously rejected and expelled into liquid ahead of the solidification front. This microsegregation at the solid-liquid interface accumulates and induces constitutional supercooling, leading to cellular or dendritic growth. Near the terminal stage of solidification, thin liquidous films with excessive alloying elements and a low melting point are present between columns or dendrites. Accompanied by the tensile stress developed in the inter-dendritic region due to thermal shrinkage (~6–8 vol percent [23]) of neighboring grains and density difference from the melt, liquid films provide easy pathways for delamination on the mushy zone and resultant so-called solidification cracks. This is exacerbated by a short lifetime (around 20 ms [24]) of liquid backfill due to the steep thermal gradient (10^4–10^6 K/s [24,25]) rendered by laser heating and high thermal conductivity. Therefore, sensitivity to solidification cracking is related to a prolonged solidification temperature range [5] and an abundance of soluble elements [2]. A criterion was proposed to quantify hot cracking susceptibility: $|dT/d(f_S^{1/2})|$ near $f_S^{1/2} = 1$, where T is the temperature and f_S is the fraction of the solid in the semisolid [22]. This model incorporates the lateral growth rate of columnar grains and length of intergranular channel for liquid backfill. A higher value implies a greater cracking tendency. With the assistance of quantitative criteria, cracking susceptibility could be depressed by fine tuning the concentration of alloying elements. This model has been successfully validated in several systems both in the context of welding [14,16] and additively manufactured Al-Cu [26], Al-Si [8] systems, and provides physical insights on chemistry determination.

Another strategy is to incorporate nucleation agents to promote equiaxial grain growth. Inoculated with ceramic nanoparticles like TiC [27–29], TiB_2 [30], or intermetallic forming elements, like Ti [31–33], Zr [34–38], Sc [39–43], Ce [44,45], heterogeneous nucleation is encouraged on the lattice-matched nucleant-Al interface on the onset of solidification. It is noticeable that the shapes of solidification curves are not substantially altered for the final stage, which would indicate little change in cracking susceptibility criterion. Instead, the high cracking resistance stems from the refined grain size and the equiaxial grain morphology that can better accommodate the solidification contraction than coarse and columnar grains, despite an unfavorable solidification ending [36].

Extrinsic approaches are also adopted to mitigate cracking, in contrast to intrinsic changes to chemistry or nucleation. Adjusting laser power, scanning speed, and defocus length could diminish cracks by changing the melt fluid dynamics from conduction mode with epitaxial-like grains to keyhole mode with refined and less textured grains, yet it is difficult to completely eliminate cracks [46,47]. Pre-heating on the build plate also decreases crack density by attenuating thermal shock and extending periods of liquid backfill due to the retarded thermal dissipation [46,48–50]. Crack curing effect starts to be perceivable at least above 200 °C [50] but preheating solely could not suppress cracking even up to 500 °C [49]. Heat retention by a thermal insulating build plate adopts a similar idea by preventing rapid cooling [33]. Notable crack mitigation is also achieved with other methods including manipulation of scanning strategies [45,51,51,52], overlap rate of adjacent laser tracks [52], specimen geometry [51], and hot isostatic pressing (HIPing) [45].

Through current strategies, identification of optimal processing parameters for defects-free high-strength Al alloys is challenging. To take advantage of high-performance alloy compositions, crack suppression strategies must be developed to determine their effectiveness and identify generalizable methods which address the most significant cracking mechanisms. Here we report a systematic crack mitigation effort through printing optimization for a custom high-strength Al alloy $Al_{92}Ti_2Fe_2Co_2Ni_2$ with nanoscale intermetallics fabricated by LPBF. Various pioneer work on additively manufactured Al–Fe–Ni confirmed that additions of Fe and Ni result in prominent precipitate strengthening and good thermal stability [1–5,7,10,11]. Ti was added for additional benefit of grain refinement and the resultant precipitate strengthening induced by primary Al_3Ti, as reported from other literature [6,8,9]. The effects of primary processing parameters (laser power and scanning speed), as well as less concerned, secondary variables, like strip length and contours, were investigated. Based on our initial findings, it was concluded that cracking may not result from either composition-induced long solidification range or liquation. Instead, cracking is associated with the pronounced residual stress. By designing a scaffold support structure that deliberately favors cracking to release residual stress, fully dense, crack-free samples could be successively printed. Our work may broaden the arsenal to address the important problem of hot cracking issue and foster a better understanding of hot cracking mechanisms in high-strength Al alloy.

2. Materials and methods

2.1. Sample fabrication

Spherical alloy powders with particle size of −53 + 15 μm (Fig. 1) and an atomic composition of $Al_{92}Ti_2Fe_2Co_2Ni_2$ were gas atomized by Atlantic Equipment Engineering, Inc.. The Back-scattered electron (BSE) micrograph for the cross sections of the powder reveals two micron-sized intermetallic compounds, acicular Al_3Ti and globular $Al_9(Fe,Co,Ni)_2$, intermingled with dark Al matrix. Phases are determined by XRD profiles (Fig. S1). Powder size distribution was constructed from analysis of 2000 particles (Fig. 1b). Most powder diameters range from 15 to 53 μm, while some small particles (below 15 μm) exist either adhering to the large powder or on their own.

LPBF was performed in SLM 125 HL with an infrared 400 W IPG laser operating at 1070 nm to print cuboid specimens with dimensions 10 × 10 × 5 mm (width × length × height). The printing process controlled Al build plate temperature at 200 °C and chamber oxygen content below 0.1% after initial ultra-high-purity Ar flushing. By default, each layer is composed of parallel laser tracks segmented into short laser strips. Layer thickness, hatch spacing, layer rotation, laser strip length (SL) were kept constant as 30 μm, 100 μm, 67°, 1 mm, respectively, unless otherwise stated, while laser power and scanning speed varied. Laser defocus (DF) denoted the perpendicular shift of focal point to the powder surface and was assigned as 0 by default. Positive DF value indicates that laser focal point is higher than powder surface. Effective beam spot expands from 66 μm for the focal plane to 84 μm, 123 μm for ± 2 mm, ± 4 mm DF, respectively. Contours (borders) are additional tracks surrounding the outer surface and were set with two layers and 100 μm interspace. The chessboard pattern (island) was also utilized for some trials. The hatch space is 100 μm, consistent with the strip pattern and each patch (island) is 2 × 2 mm. Printed samples were sectioned off the plate by wire electrical discharge machining with a Mitsubishi FX-20 K machine. Vickers hardness testing was carried out with a load of 100 gf and a holding time of 10 s. Physical values were averaged from 20 measurements for each parameter set.

To probe the processing window, frequently considered parameters include laser power (P), scanning speed (v), hatch space (h) and layer thickness (t). A derivative variable, volumetric energy density (VED), integrates these four parameters into one single formular (1) and estimates energy input for a given unit volume.

$$VED = \frac{P}{v \cdot h \cdot t} \tag{1}$$

2.2. Microscopy analysis

Optical microscopy (OM) and scanning electron microscopy (SEM) images were collected on an Olympus SZX7 and a Thermo Fisher Quanta Field Emission Gun (FEG) 650 microscope. All the samples were ground with SiC abrasive papers down to P-4000 grade, and polished with 1 μm

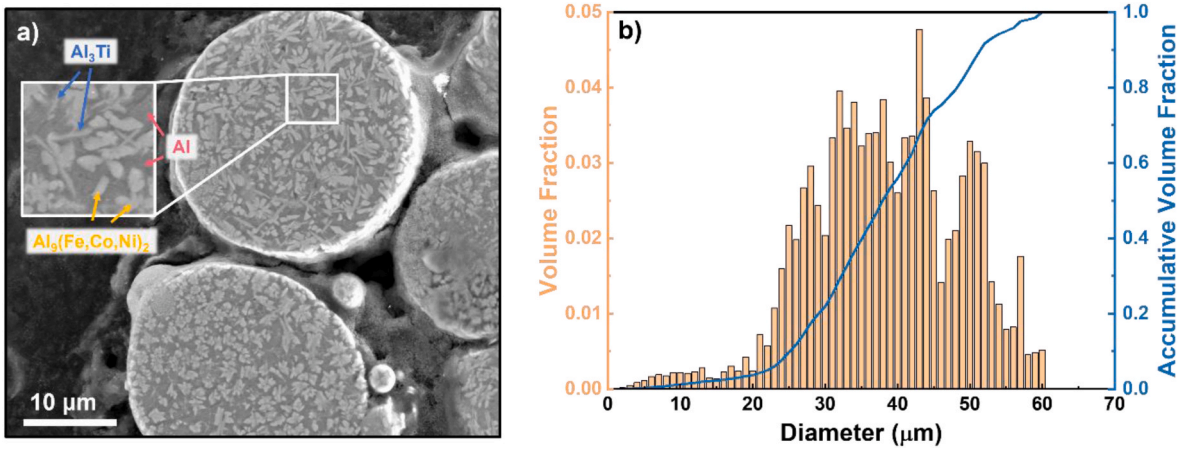

Fig. 1. (a) Cross-section morphology of the gas atomized $Al_{92}Ti_2Fe_2Co_2Ni_2$ alloy powder. The insert shows two forms of intermetallic compounds, acicular-Al_3Ti, globular-$Al_9(Fe,Co,Ni)_2$ in Al matrix. (b) Particle size distribution of $Al_{92}Ti_2Fe_2Co_2Ni_2$ powder.

diamond paste before microscopy study. The total removal was at least 300 μm of material on each surface of interest. BSE detector and secondary electron (SE) detector were utilized for probing the z-contrast microstructure and fractography. TEM micrographs were captured in a Thermo Fisher Talos 200X TEM with an acceleration voltage of 200 kV.

Crack density is defined as ρ = total crack length / surface area (m/m^2). Crack density statistics were measured in a semi-automated workflow consisting of extensions in the Fiji (Fiji is just ImageJ) software based on OM image inputs (Fig. S3a) [53]. OM images were binarized using a greyscale threshold to isolate the crack network. Pixels in the network were dilated several times to connect cracks separated by thresholding. The "skeletonize (2D/3D)" extension [54] was used to generate the crack network (Fig. S3b) and then the "Ridge Detection" extension [55] broke down the network into measurable line segments (Fig. S3c). A line segment analysis tool was used to sum the segment lengths above 0.1 mm to exclude confusion with porosity contrast. This semi-automated method minimized manual measurement error.

2.3. Residual stress measurement

X-ray diffraction (XRD) measurements were conducted on a PANalytical Empyrean X'pert PRO MRD diffractometer with a 2 × Ge (220) hybrid monochromator to select Cu Kα1 in the $2\theta - \omega$ geometrical configuration. Residual stress was derived from the peak shift using the $\sin^2\chi - D$ method [56] in the laser track transversal and longitudinal directions on the bottom surface of the cuboid sample. χ denotes the tilt angle for the normal vector of the measured surface relative to the goniometer circle plane, and D denotes crystallographic planar spacing. Al (311) was selected because peaks with higher Bragg angle are more sensitive in response to residual stress, and the Al (311) peak does not overlap with precipitate peaks in this alloy. Peak positions were measured for $\chi = 0°$, 18.44°, 26.57°, 33.21°. The residual stress could be calculated by the following equation (2),

$$\sigma_{residual} = \left(\frac{\partial D}{\partial(\sin^2\chi)}\right)\left(\frac{E}{1+\nu}\right)_{(311)}\left(\frac{1}{D_{(311)}}\right) \quad (2)$$

where elastic modulus normal to Al (311) planes $E_{(311)}$ = 72 GPa, Poisson's ratio ν = 0.33, Al (311) interplanar spacing $D_{(311)}$ = 1.2210 Å [56].

2.4. X-ray microscopy

X-ray microscopy (XRM) was conducted with a Zeiss Versa 620 lab-scale x-ray tomography system to examine cracks and porosity in three dimensions. Samples of interest were ground to a square cross section of 20.25 mm^2 orthogonal to the plane of the baseplate. Samples were then scanned with the cross section's normal plane oriented vertically. Scans were conducted with the samples 14 mm from the x-ray source and 12 mm from a detector with 4× optical magnification, giving a final voxel size of 3.65 μm. To capture the full sample volume, a wide view scan strategy was applied, whereby the sample axis was shifted and rotated to produce two scans with extended field of view, which were then stitched automatically by the system's built-in software. Additionally, the top and bottom halves of the samples were scanned separately then stitched using tomography system software. As a result, the field of view was extended to 450 × 450 × 484 μm.

Filtering of the 3D tomography data was done in Avizo 9 (Thermo Fisher Scientific). A median smoothing filter was first applied to reduce noise, followed by a nonlocal means smoothing filter to produce distinct grey values for voids and the alloy. Last, an unsharp mask filter was applied to highlight edges, resulting in minimized noise and sharp edges between the metallic matrix and defects. Segmentation was then performed manually to separate the alloy matrix, cracks, and pores into distinct label groups. A greyscale threshold was used to identify the matrix, and pores were segmented based on size. Thin cracks and pores contacting cracks were segmented using a brush tool. Measurements of the segmented features were performed as voxel counts of connected volumes.

3. Results

3.1. Single track observations

Single laser track experiments were conducted as a common practice to probe the processing window prior to actual printing the customized $Al_{92}Ti_2Fe_2Co_2Ni_2$ alloy. Large variations of laser power (ranging from 25 to 370 W) and scanning speed (ranging from 100 to 3000 mm/s) were explored for a thorough understanding of the melt pool behaviors. Three regions were determined in Fig. 2a: 1) a balling region, characteristic of unstable fluid dynamics and resultant discontinuous melt beads, 2) a conductive region with tracks of consistent width and stable fluid dynamics, and 3) a keyhole region, overheated by high energy input, leading to broad tracks with cavities beneath the surface as confirmed by cross section SEM (not shown in the paper). It is also found that the melt pool expands both horizontally and perpendicularly as VED escalates (Fig. S2), increasing the aspect ratio (depth/width). It is worth mentioning that all laser tracks do not exhibit any cracks under SEM. Subsequent printing experiments aimed primarily at the conductive region with reasonable VEDs as well as some marginal balling and keyhole region.

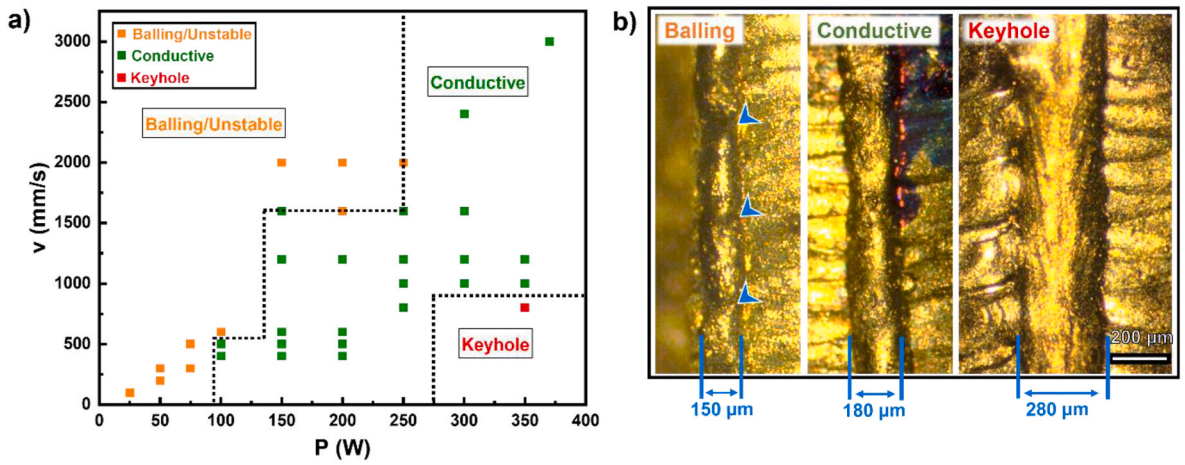

Fig. 2. (a) Single laser tracks indicating three regions of melt pool dynamics: balling/unstable, conduction and keyhole regions. (b) Top-down views showing the morphologies and widths of the representative laser tracks for each region. Balling: 250 W, 2000 mm/s; Conduction:250 W, 1200 mm/s; Keyhole: 350 W, 800 mm/s. Blue arrows indicate the discontinuous beads which do not form as a regular track. (For interpretation of the references to colour in this figure legend, the reader is referred to the Web version of this article.)

3.2. Impacts of primary parameters

Extensive optical microscopy images were collected for the specimens printed with the default strategy for a wide range of laser power and scanning speed (Fig. 3). Two major classes of defects, solidification cracks (white lines) and pores (white speckles), were identified from the optical images. Cracks formed as an inter-connected network terminated on the side surfaces. No significant orientation dependence was observed for cracks. The relevant statistics were performed using the computer-aided method (Fig. 4). A clear trend of defect populations was observed with respect to VED. As VED increased from 20 to 170 J/mm^3, i.e., higher laser power or lower scanning speed, crack density monotonically decreased from 3000 to 250 m^{-1}. No parameter set within the investigated scope was capable of producing crack-free samples. In

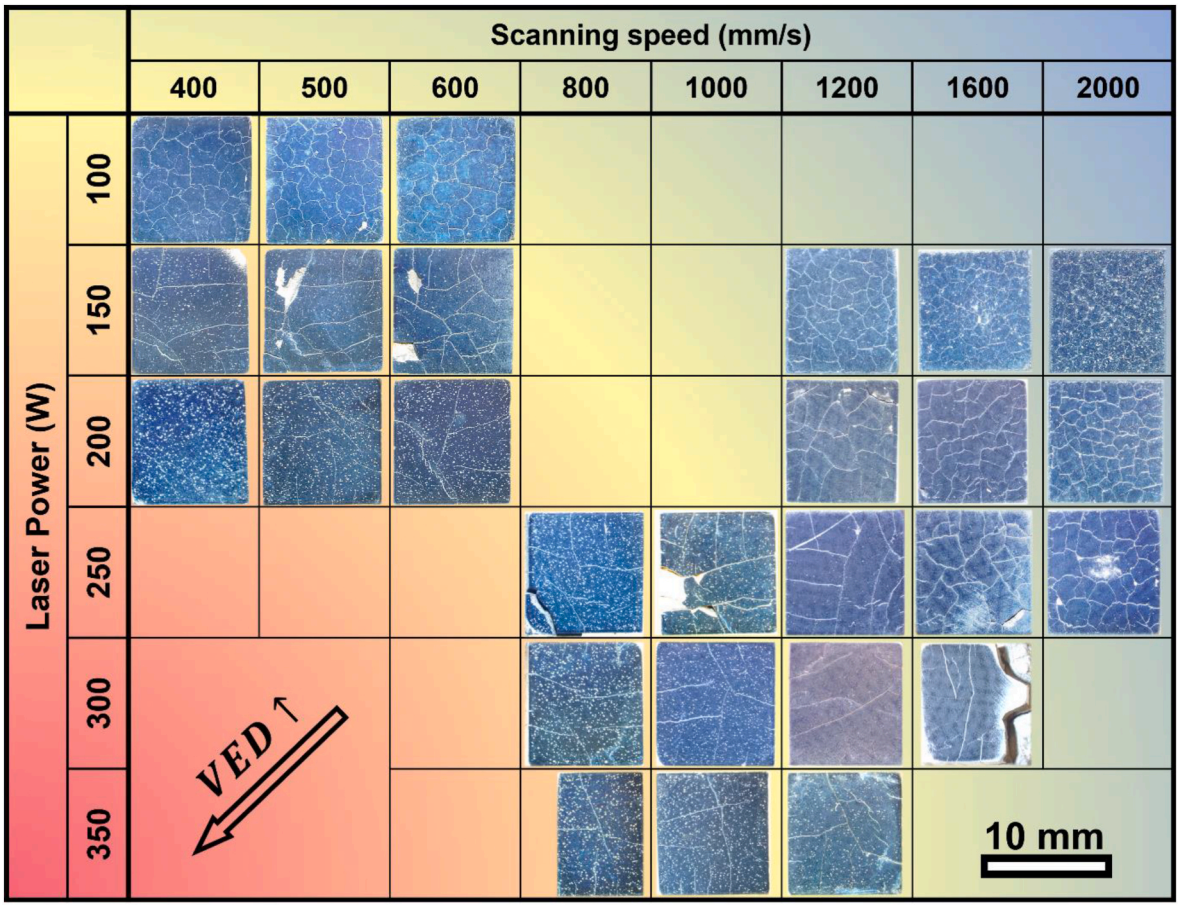

Fig. 3. A panoramic view of optical microscopy images for the bottom surface of samples printed with various laser powers and scanning speeds. The lower left corner represents a high volumetric energy density (VED).

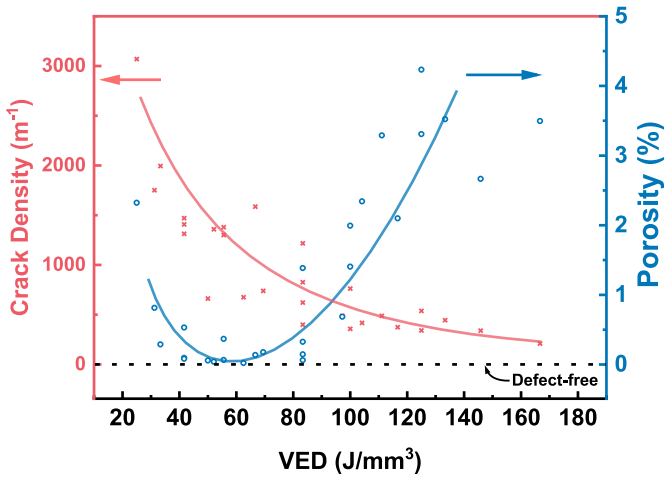

Fig. 4. Statistics on evolution of porosity and crack density with VED. Crack density monotonically decreases with increasing VED, but cracks can not be fully eliminated within the investigated range. Porosity reaches a valley at around 60 J/mm^3.

comparison, porosity reached a minimum, being nearly porosity-free at intermediate VEDs (around 60 J/mm^3) and then rose to 4% at high VEDs. Lack-of-fusion pores with an irregular shape dominate at low VEDs whereas nearly spherical keyholes appeared at high VEDs. As such, VED could not be increased to reduce cracking further without introducing destructive quantities of keyhole pores. Routine parameter optimization on laser power and scanning speed could not yield fully dense and crack-free samples fulfilling structural applications.

Vickers hardness measurements in Fig. 5 demonstrate the high hardness of this alloy, ranging from 160 to 250 HV. The hardness is generally inversely related to VED and seems to be more dependent on laser power rather than the scanning speed. Samples printed with varying VEDs appear to have very close phase constituents (Fig. S1).

Fig. 6 presents images and micrographs of the specimen (10 × 10 × 5 mm) printed with adequate laser power (P = 250 W, v = 1200 m/s, VED = 69 J/mm^3) based on the porosity curve in Fig. 4. The integrity of geometry was maintained despite minute warping and peeling-off on the bottom. Cracks and pores are highlighted on the optical microscopy

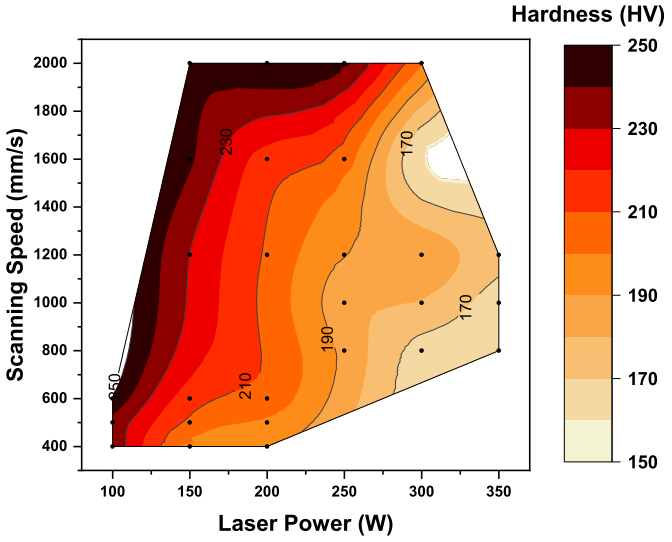

Fig. 5. Vickers hardness evolution of the as-printed samples with respect to laser power and scanning speed. Parts printed with all the parameter sets show a high hardness ranging from 160 HV to 250 HV. Hardness is inversely related to the VED value.

images (Fig. 6b and c). It could be seen from the side surface that most cracks are major and propagated to the top surface, whereas occasionally there are some minor cracks terminated in the interior. On the bottom surface, minor cracks appear near the contour region and get terminated. Cross-sectional SEM images (Fig. 6d and e) reveal a heterogeneous microstructure, consisting of intermetallic colonies in Al matrix. Primary cracks penetrated multiple weld tracks with melt pool boundaries denoted in pink. Along the pathway of cracks, some intermetallic rosettes cracked internally, while most intermetallic rosettes deflected cracks into the Al matrix. In images of a crack tip taken on the xy plane (Fig. 6f), a broad crack is split into several insignificant vanishing microcracks, resembling a river delta. A top-down view of the crack surface in Fig. 6g shows a rough, irregular texture with "cups and cones" morphology.

A detailed characterization of the microstructure reveals two alternating morphologies in Fig. 7. An SEM micrograph near the melt pool boundary (MPB) shows the representative constituents in the coarse rosette region and the fine rosette region. Coarse rosette regions are composed of two types of intermetallic laminates (Al_3Ti and $Al_9(Fe, Co, Ni)_2$) and cellular Al matrix (Fig. 7b). It is also found that minor eutectic intermetallics decorate the cellular boundary. Whereas fine rosette regions contain much more refined intermetallic lamellae ($Al_3Ti/Al_9(Fe, Co, Ni)_2$) surrounded by a small amount of Al (Fig. 7c). The partitioning and mechanical behaviors of these intermetallic precipitates are discussed elsewhere.

3.3. Impacts of the secondary parameters

Given undesirable quantities of either cracking or porosity after attempting to optimize laser power and scanning speed, the effects of other processing parameters on crack mitigation were investigated to mitigate cracking. These parameters included scanning strip length (SL), contours (vs no contours), defocus length of laser (DF), scanning pattern, and dimensions of samples. Three VEDs were selected from the low porosity VED range in Fig. 4. These represent three scenarios: slightly underheated "V50" (P = 300 W, v = 2000 mm/s, VED = 50 J/mm^3), intermediate "V69" (P = 250 W, v = 1200 mm/s, VED = 69 J/mm^3), and slightly overheated "V83" (P = 100 W, v = 400 mm/s, VED = 100 J/mm^3) in reference to the VED with minimal porosity around 60 J/mm^3. Specimens were fabricated by varying the default parameters one at a time to study individual parameters' effects. Optical micrographs were collected for plan-view and cross-section of the specimens as shown in Fig. 8 and Fig. S6. The measured crack densities are then presented for the planviews and side views in Fig. 9, with horizontal lines drawn to show the crack densities measured for default parameters. The complex effects of these various parameters result in both positive and negative changes in crack density.

SL is set to 1 mm by default and was varied to 10 mm and 15 mm. In the 1 mm situation, the laser repeatedly activates, writes short strips, diminishes, and re-activates across a single track. Given a scan strategy rotated with respect to the cube edges, the longest cube dimension is the corner-to-corner diagonal, which is 14.4 mm. Thus, a 15 mm strip length is required to scan from end to end in a single scan track. A 10 mm strip length is intermediate. For the three VED settings, crack density decreases on the side surface with longer strip lengths but increases on the bottom surface.

As for contours, removing contours for three VEDs is beneficial in cutting down crack density on both planes, especially for V69 (Fig. 9b) which gives minimal crack density among all the trials.

Laser defocus length varied from 0 to ± 2 mm and ± 4 mm and its effect on crack density seems to depend on VED (Fig. S6). As for underheated "V50" (Fig. 9a), all four defocus distances produced a higher crack density compared with the default one. Focal plane shifts exacerbated cracking on both surfaces, and larger shifts led to worse cracking. The effects of opposite signs of DFs are symmetrical given the same values. However, as for overheating "V83" (Fig. 9c), all DF

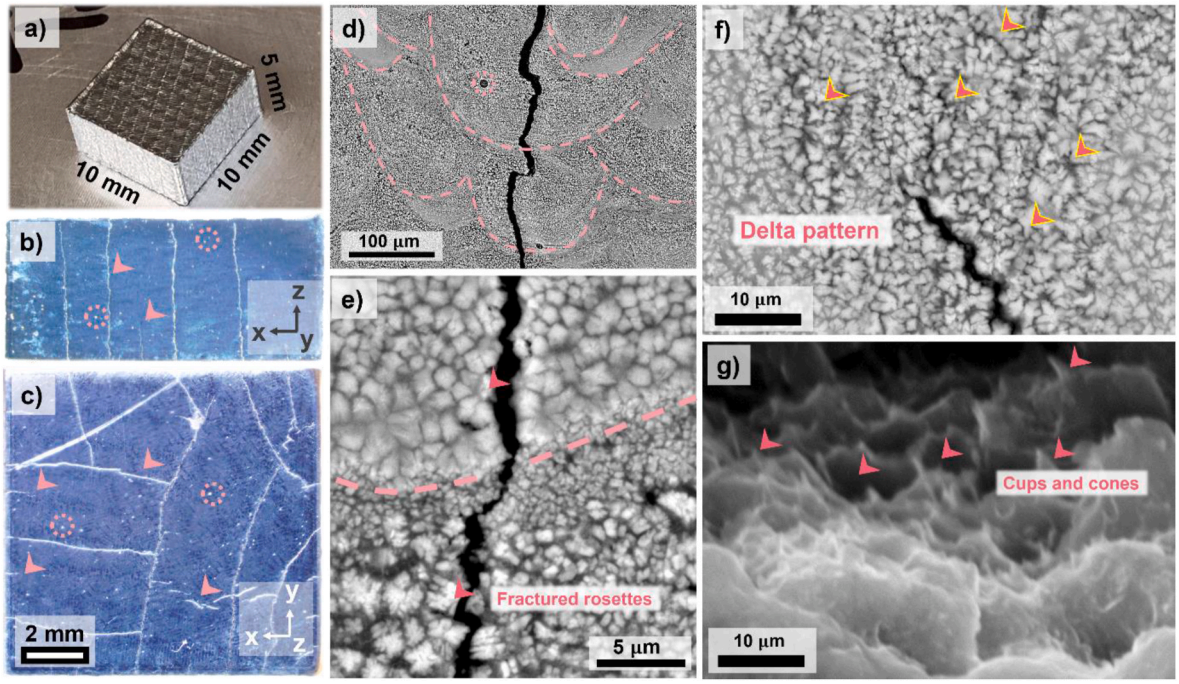

Fig. 6. (a) An optical image of the sample printed with 250 W laser power and 1200 mm/s scanning speed. (b, c) The corresponding stereo microscopy images on the polished side surface and bottom surface showing cracks (indicated by red arrows) and pores (dotted circles). (d) A backscattered SEM micrograph showing the crack propagated across multiple melt pool boundaries (shown by pink dashed lines). (e) An SEM micrograph for the crack near the melt pool boundary with some fractured rosettes. (f) A relatively wide crack is terminated with traces of microcracks resembling the delta pattern at the end of rivers. (g) A micrograph showing the magnified view of the cracks with "cups and cones" morphology. (For interpretation of the references to colour in this figure legend, the reader is referred to the Web version of this article.)

distances reduced cracking. Crack density changed inconsistently with varied DF settings, however. Mixed effects of DF on cracking were observed for "V69" (Fig. 9b).

Another considered parameter was scanning pattern. The influences of two common patterns, chessboard and strips, on crack density were tested. Crack density decreased for "V50" and "V69" but increased for "V83" when a chessboard pattern was used. Besides, small samples printed with dimensions 6 × 6 × 3 mm showed increased cracking for "V50" but decreased cracking for "V69" and "V83" (Fig. S6). In summary, secondary parameters could greatly influence the crack populations, and the modification of certain parameters will reduce cracks; but they can not completely eliminate cracking.

3.4. Residual stress analysis

To resolve the mechanism of solidification cracking, one specimen "V69" following the default print strategy was printed but with no layer rotation, no contour, and 15 mm SL. The polished bottom surface was imaged and is shown alongside the bi-directional scanning strip vectors in Fig. 10a. It is intriguing that most cracks denoted with blue arrows extend orthogonally to the laser scanning direction. An SEM micrograph (Fig. 10b) confirms that cracks opened through laser weld tracks in the longitudinal direction. X-ray analyses characterized the normal residual stress in both transversal and longitudinal directions (Fig. 10c–f). Surprisingly, significant tensile residual normal stress is present in both directions and values can be around 1 GPa and 500 MPa in transversal σ_T and longitudinal σ_L directions, respectively.

3.5. Scaffold structure

Inspired by the alleviated residual stress as a consequence of crack generation, compartmentalized support structures were designed to relax residual stress by intentionally favoring distortion or even cracking formation. Three representative support variants, which include two waffled lattices with different cell sizes and one with pillar arrays, were designed for this purpose and their efficacy is shown in Fig. 11. These supports have a wide span of density, with A being the most compact and C being the most open.

Only one design successfully survived printing and produced parts with various geometries (Fig. 12). A schematic in Fig. 12a demonstrates the detailed structure of this scaffold support. The support is comprised of multiple duplicated 1.5 × 1.5 mm cells, and each cell is composed of intersecting vertical thin platelets with 0.2 mm interspace, which mimic the hatched walls of a waffle. In contrast to the hatch space of 0.1 mm producing solid parts, this doubled hatch space of 0.2 mm intentionally builds cavity arrays into the support structure. Each platelet is 1.5 mm wide and chamfered on the four corners. Between every neighboring two "waffle" cells, there are run-through channels with a width of 0.2 mm. Cuboidal specimens were printed on top of these "waffle islands." Optical images in Fig. 12b show that prominent distortion is present in the "waffle islands", which are designed to be straight and perpendicular. A closer view in the insert reveals that curvature (denoted with red dashed lines) for platelets seems to escalate inside each cell, reset, and iterate this pattern among cells. Cavities (black vertical lines) where inter-cellular channels intersect the side surface are also observed. Some delamination happens to the bottom joint interface. Beyond cuboidal samples, crack-free cylindrical bars and vertical slabs were successfully printed with the support structure without visible surface cracking (Fig. 12c).

3.6. Scaffold imaging

Side surfaces of cuboidal samples on support structure were polished, and no visible cracks were found under SEM. However, internal cracks may occur and still jeopardize the mechanical performances. Two samples of the same laser power 250 W and scanning speed 1200 mm/s (V69) were printed with and without the support structure (denoted "support" and "control", respectively). Internal voids in these two

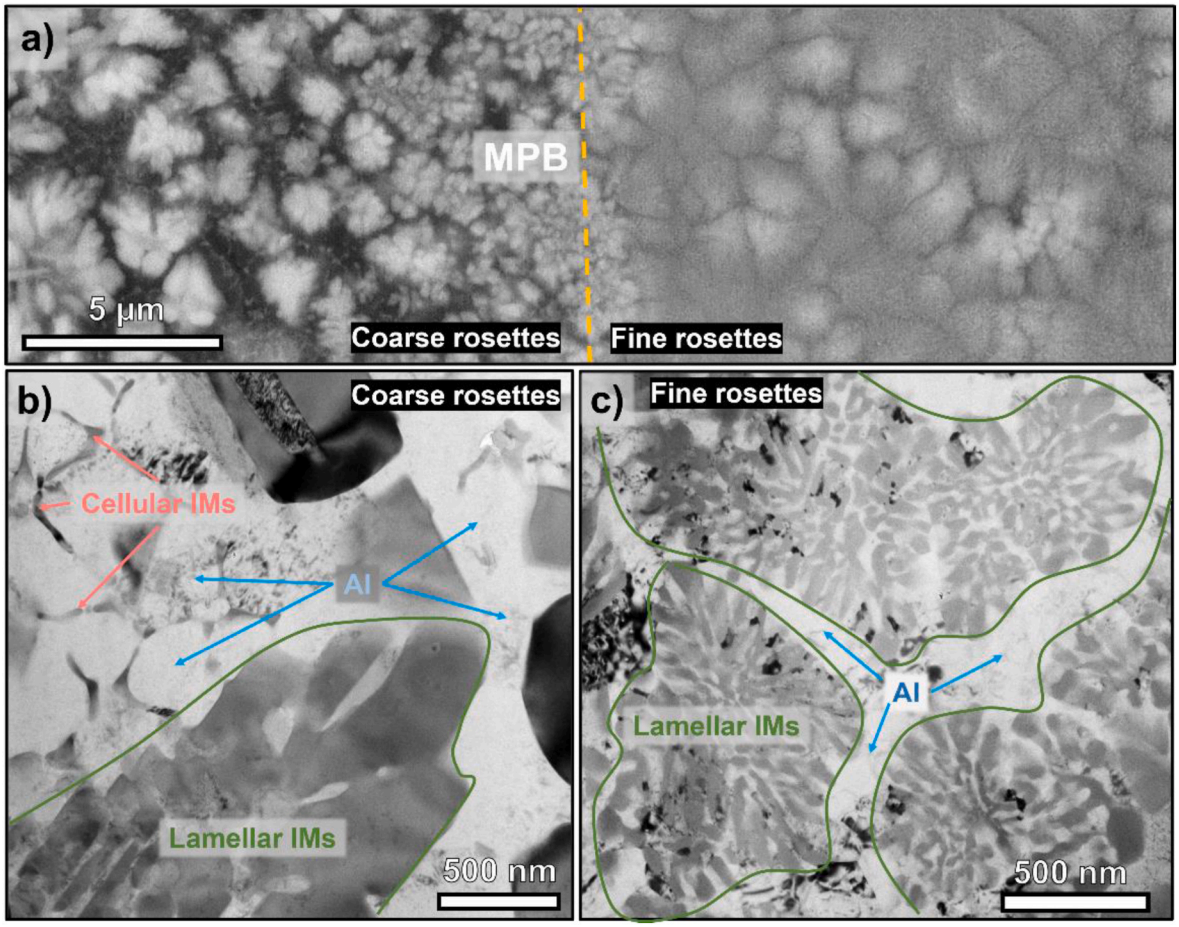

Fig. 7. (a) An SEM micrograph on the melt pool boundary (MPB) in the as-printed state, revealing the heterogeneous microstructure: coarse rosette region and fine rosette region. The laser power and scanning speed are 300 W and 1200 mm/s, respectively. (b) A TEM micrograph on the coarse rosette region, which is composed of relatively thicker lamellar intermetallics, cellular intermetallics and Al matrix. (c) A TEM micrograph showing the fine rosette region, which is composed of intermetallics nanolaminates surrounded by Al.

samples were studied with x-ray computed tomography in Fig. 13. From the cross-section views and backward-forward rendering views, the control sample contains multiple large vertical cracks, and some cracks extend to the top surface (Fig. 13ab), which is consistent with the optical microscopic observations. However, the support sample only exhibits cavities below the scaffold, and no cracks are found in the actual part (Fig. 13de). Bottom-up projections confirm cracking in the control sample (Fig. 13c). Fig. 13f shows the designed "waffle islands" structure is properly rendered in the support sample. Small pores are left between vertical platelets inside cells, while large cavities form at the intersections of inter-cellular channels. Channels connecting large cavities seem to be highly deformed and tortuous, which verifies the compliance of the support structure. Support is not only preferred for crack elimination, but also for densification (Fig. S4). Porosity dropped from 0.19% for the control sample to less than 0.1% for the support sample (Fig. S4a and b). Pore diameter follows a lognormal distribution for both samples, and the mean pore diameter shrank from 11.9 μm in the control sample to 6.6 μm in the support sample (Fig. S4c).

To examine how the compliant support structure interacts with the cracking, horizontal cross sections at different heights are presented in Fig. 14. In general, cracks fade away rapidly with a reduction in both gap width and density, as the height increases. In the vicinity of the bottom surface (in contact with build plate), cracks are large and generally follow the perpendicular orientations of the inter-cell channels. Cracks are fairly tortuous, and some propagate into cells and connect to small pores (Fig. 14b). At the height of 1 mm, cracks inside cells seem to disappear and channel crack density diminishes as well (Fig. 14c). Intracellular channels are visible as powder-filled voids. Higher in the scaffold, channel cracks almost vanish, too (Fig. 14d). Near the top of the scaffold, it becomes difficult to distinguish cracks among the intercellular channels, and the centers of the "waffle islands" become fully dense (Fig. 14e). When it approaches the sample interior, cracks are fully eliminated (Fig. 14f).

4. Discussion

4.1. The effects of printing parameters on crack mitigation

Processing window assessment of this custom Al alloy began with single laser track experiments for high efficiency screening, a strategy that has been demonstrated previously [51,57,58]. The main purpose of the single laser track studies is to exclude any unstable or defective tracks to prevent defect accumulation. Cube specimens printed with relatively low and high VEDs will manifest lack-of-fusion pores and near-spherical keyholes inherited from the single tracks, respectively, which are reflected in the high porosity at two VED extremities (Fig. 4). An increase in the melt track aspect ratio (Depth/Width) also corroborates the transition of melt pool dynamics from the conduction mode to the keyhole mode as VED increases (Fig. S2). Conduction melting is preferred, though slight shifts toward keyhole mode were found to reduce crack sensitivity [46]. However, printing reliability is not fully guaranteed by proper parameter sets evaluated by single laser track morphology due to track interplay. The overlap region between adjacent tracks could undergo multiple stages of annealing, partial melting, or

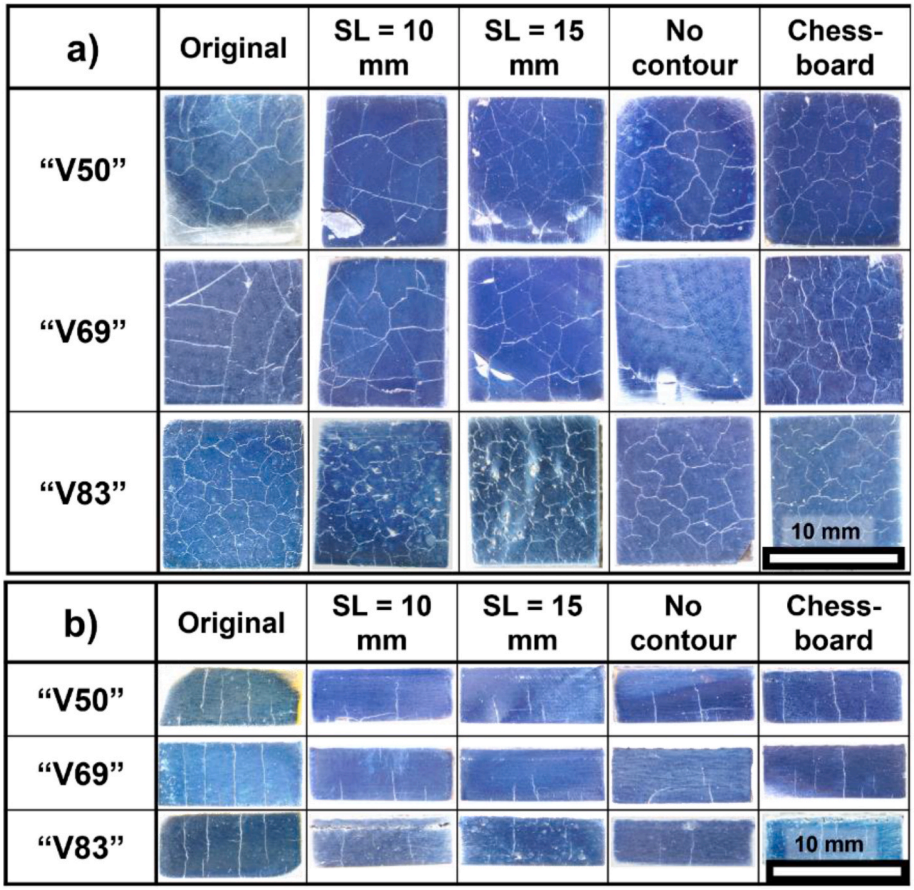

Fig. 8. An optical microscopy image collection for (a) the bottom surface and (b) the side surface of samples printed with three selective VEDs and varying secondary laser processing parameters: “V50”, P = 300 W, v = 2000 mm/s, VED = 50 J/mm^3; “V69”, P = 250 W, v = 1200 mm/s, VED = 69 J/mm^3; “V83”, P = 100 W, v = 400 mm/s, VED = 100 J/mm^3; “SL = 10”, 10 mm laser strip length; “SL = 15”, 15 mm laser strip length; “Chessboard”, chessboard scanning pattern. Specimens were fabricated by varying the default parameters one at a time so as to study individual parameters’ effects on defect density.

full remelting. A thermal history which includes multiple temperature spikes, in contrast to the single spike of a single track, may give rise to the cracking observed in most of the samples shown in Fig. 3. In spite of the prevailing cracks, higher VED (higher laser power or lower scanning speed) would reduce crack density, due to attenuated thermal shock, longer duration for liquid backfill and reduced residual stress. It is interesting to notice this crack alleviation phenomenon by higher VED is different from what has been reported in AM AA 7075 [50] and AA 2024 alloys [52], implying the existence of an alternative cracking mechanism. A proper range of VED, ~60 J/mm^3, is identified for providing minimal porosity (Fig. 4). However, in such conditions, there is still cracking, as crack density decreased monotonically with increasing VED. It is evident from Fig. 4 that tailoring VED alone is insufficient to remove porosity and cracks simultaneously to achieve near full density.

The effects of other printing parameters (strip length, contour, and defocus) on crack density are revealed from the qualitative and quantitative views of numerous samples in Fig. 8, Fig. S6 and Fig. 9. Stripe length shows anisotropic impacts on crack density on the xy and yz planes. Compared with the samples printed using a strip length of 1 mm, increasing the strip length to 10 or 15 mm decreases crack density on the yz plane but increases crack density on the xy plane. The reduced crack density on the yz plane is manifested from shorter crack propagation paths. A likely explanation would be that less frequent pauses and reheating by using longer strip lengths would impose fewer recurring thermal shocks and could lead to reduced cracking, as witnessed on the yz plane. Though the crack density surges on the xy plane, smaller crack gap separations are indicated by less defined and faint cracks. The contour strategy is commonly used for better surface finishing, as the perimeters of a part are printed first to achieve a rigid and well-defined surface, followed by the fill of the built interior. The removal of contours (NC) has a beneficial effect to crack mitigation as observed in all VEDs (Fig. 8), and the NC strategy is more prominent in the “V69” group. Contours seem to trigger cracking from the periphery where contours join with interior laser tracks and deteriorate printability (as shown in Fig. 6c, which was printed with contours). It is postulated that cracking may partially result from the inability for stress relaxation due to structural confinement imposed by contours. For this custom Al alloy, densification could be partially improved by fine tuning defocus for certain groups of specimens, such as “V69” (Fig. 9b) and “V83” (Fig. 9c). However, the effect of defocus on crack reduction in the “V50” group (Fig. 9a) is inconclusive. Defocus redistributes the laser energy flux and could change the melting modes. Keyhole melting with a tapered melt pool morphology could be obtained by a negative defocus distance, which enhances crack resistance as evidenced by previous reports [46,59]. Chessboard scanning pattern and smaller dimensions seem to have an ambiguous effect on cracking.

4.2. *The mechanisms of hot cracking*

Hot cracking in aluminum is generally considered as an interplay of several factors, such as constitutional liquation, dendritic growth and residual stress. Various mechanisms were proposed to account for hot cracking, including the prevailing solidification cracking and liquation cracking mechanisms in Al alloys. These two mechanisms may not be mutually exclusive, as initiation of one could foster the occurrence of the other mechanism [16,60]. In what follows, we will show that the

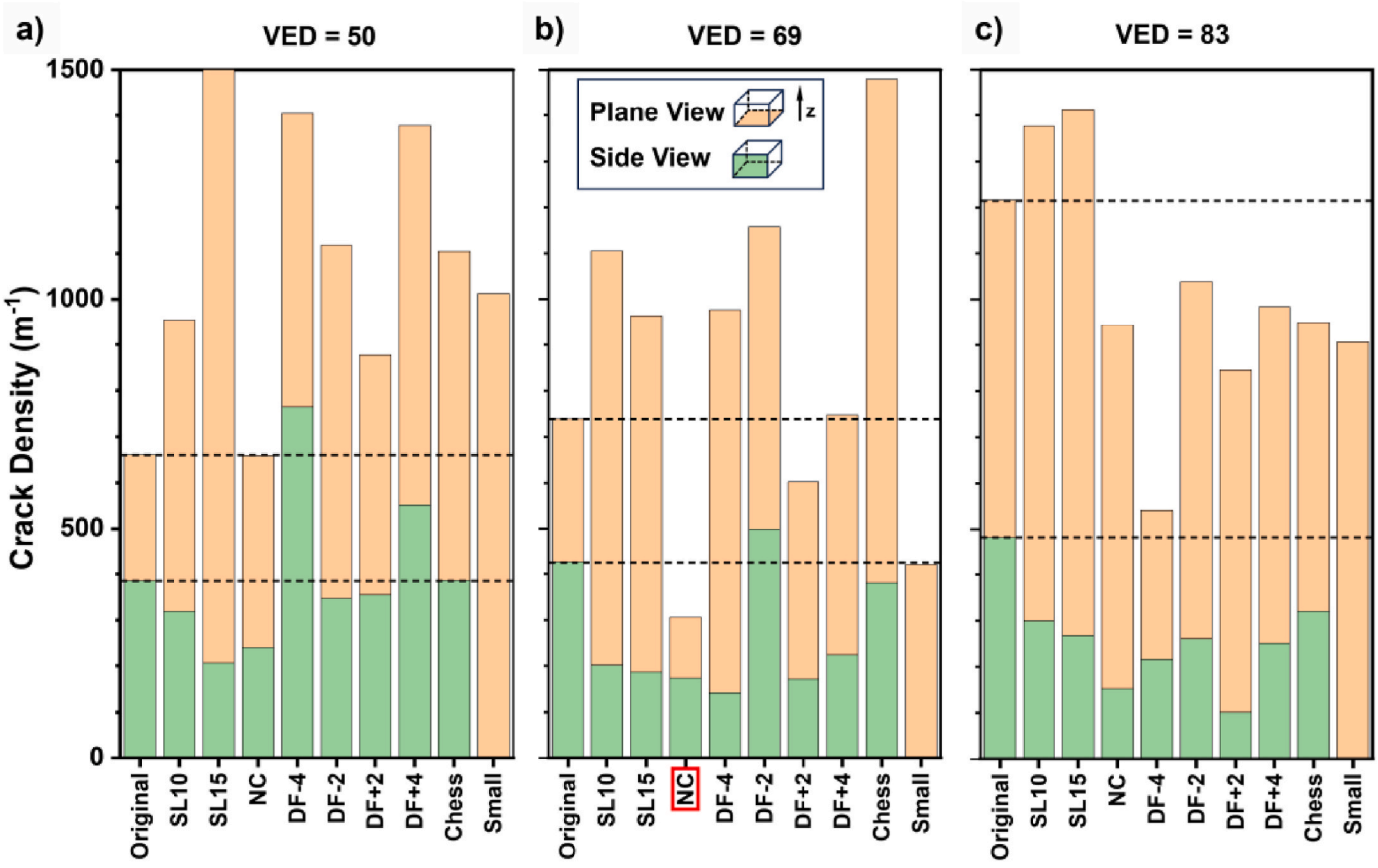

Fig. 9. Statistics of crack density in specimens fabricated with the three selected VEDs and varying secondary parameters in Fig. 8 and Fig. S6. (a) VED = 50 J/mm^3; (b) VED = 69 J/mm^3; (c) VED = 83 J/mm^3. Orange bars – crack density on the bottom surface; green bars – crack density on one side surface. Horizontal dashed lines are drawn for easy visualization of crack density change in reference to the original printing strategy. NC – No contour. All other specimens were printed with contours. The red box in (b) highlighted that "no contour" appears to be the most effective strategy for mitigating cracking. (For interpretation of the references to colour in this figure legend, the reader is referred to the Web version of this article.)

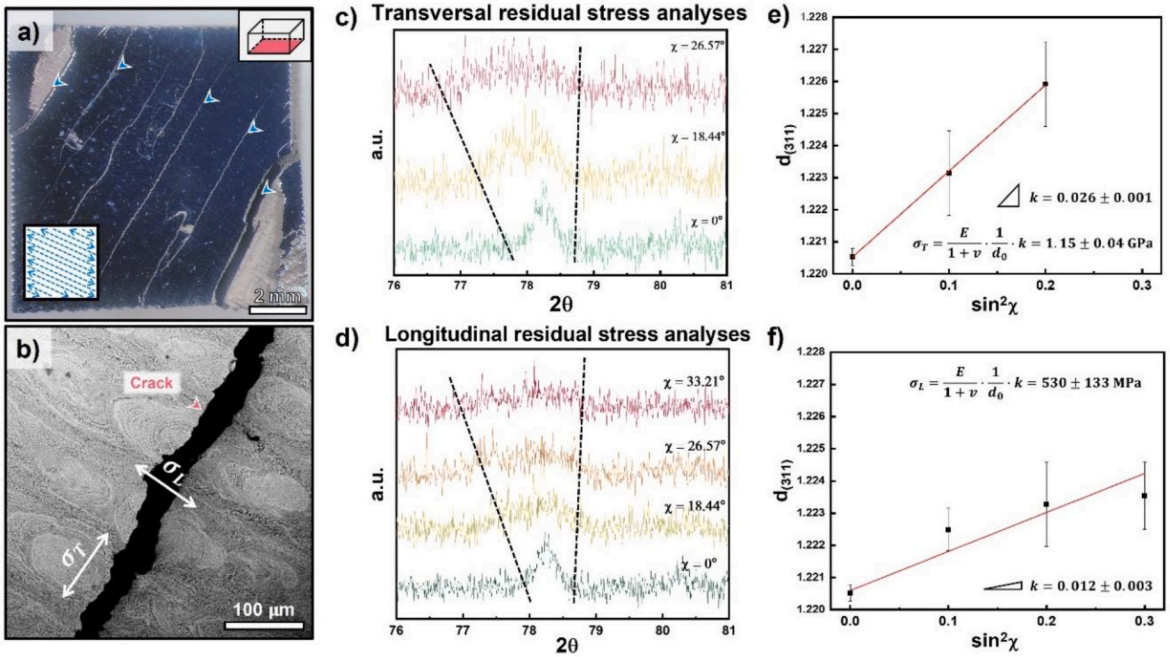

Fig. 10. (a) An optical image of the bottom surface of the specimen printed without laser path rotation every layer. The insert shows the bi-directional scanning tracks. (b) An SEM micrograph for the crack. Analyses based on sin^2 χ-d method reveal residual stress components in (c,e) transversal and (d,f) longitudinal directions.

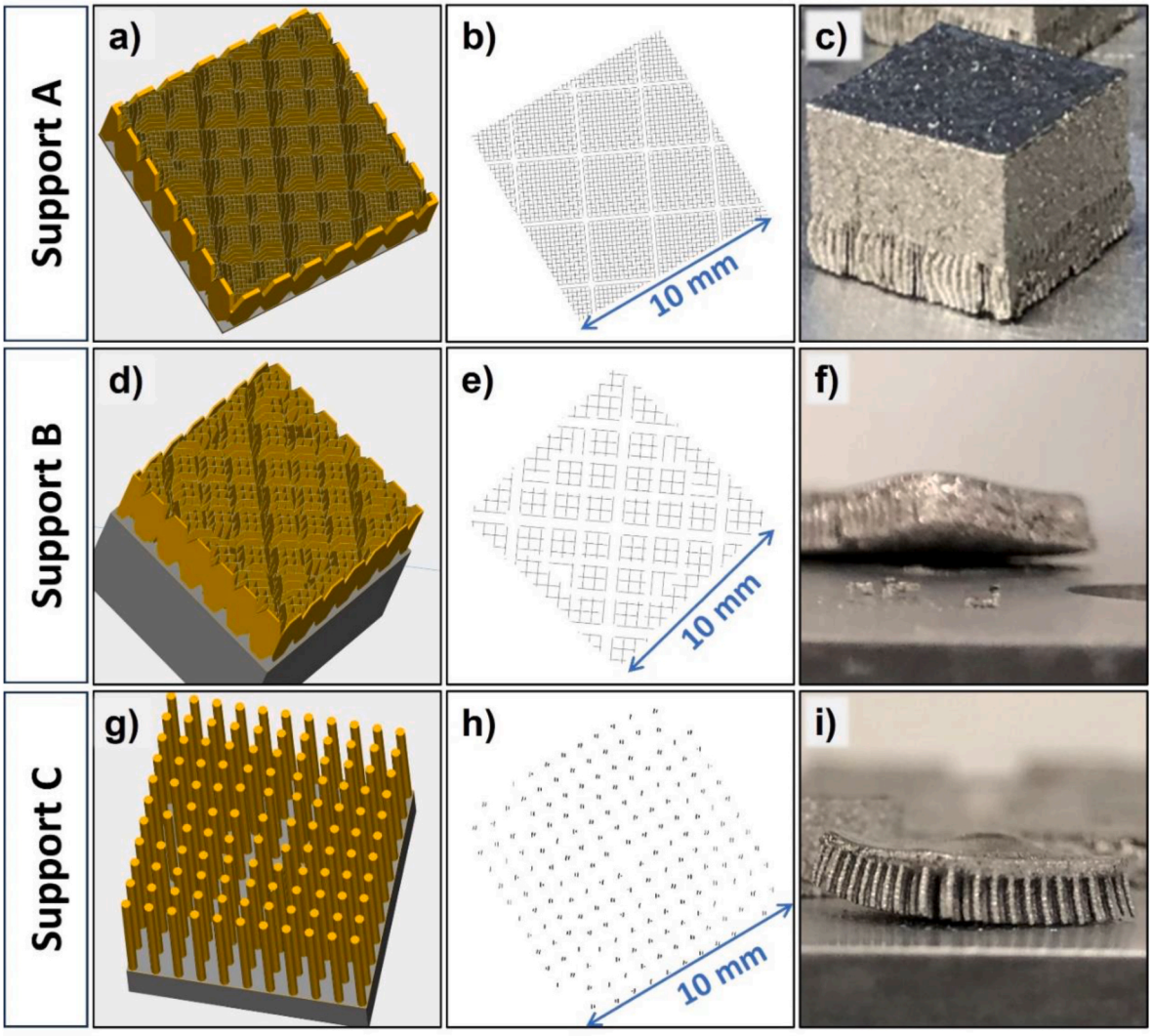

Fig. 11. Three different designs of support structures and their printability. (a) A thin-walled support "A" with 0.2 mm hatch space for platelets. (b) A schematic diagram showing the projection of support "A" along the building direction. (c) An optical image showing the printed part on support "A". Support "A" is the design shown in Fig. 12a. (d) Another thin-walled support "B" with 0.4 mm hatch space for platelets and (e) its corresponding projection. (f) Printing failed due to the severe warpage on support "B". (g) A discontinuous support "C" with arranged pillars and (h) the corresponding schematic diagram for laser tracks on one layer. Pillars were spaced by 1 mm and their diameter was 0.2 mm. One or two short tracks were rendered for each pillar. (i) Parts printed on support "C" failed due to warpage and delamination.

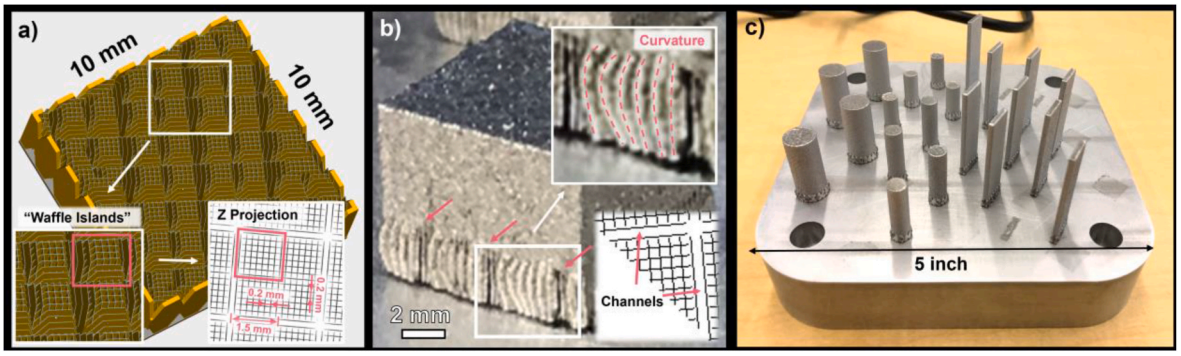

Fig. 12. (a) A schematic on the support structure design (Support A in Fig. 11) resembling "waffle islands". Each "island" is 1.5 × 1.5 mm (red square), 0.2 mm apart, composed of crisscross platelets. Four "islands" form a unit, and units are spaced by 0.2 mm. The lower right insert shows its projection along the building direction. (b) An optical image on the specimen printed with the support structure. The open vertical cavities (shown by pink arrows) are where inter-island channels intersect with the surface. A visible curvature pattern is witnessed for "waffles" in a periodic manner (insert). (c) An overview of specimens of various geometries successfully printed on the support structure: large cylinders, 10 × 10 × 20 mm; small cylinders, 6 × 6 × 12 mm; sheets 2 × 10 × 35 mm. No cracking was found inside these samples after grinding and polishing. (For interpretation of the references to colour in this figure legend, the reader is referred to the Web version of this article.)

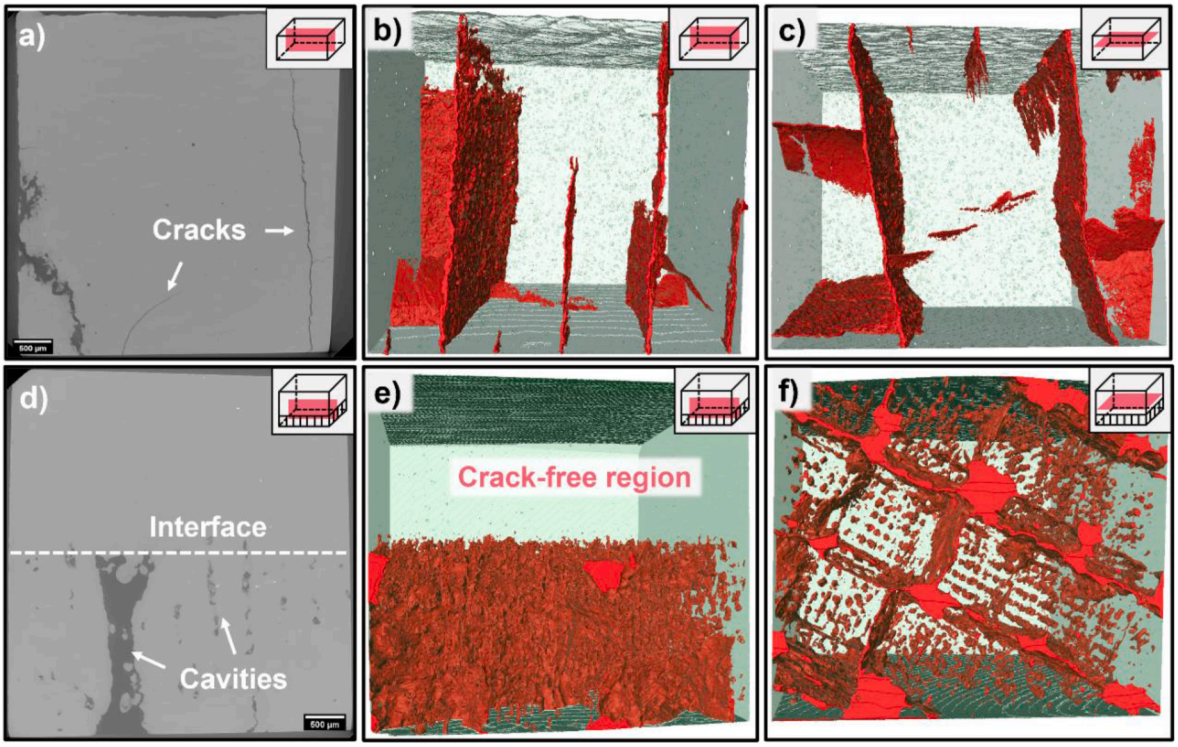

Fig. 13. X-ray micro-CT (XCT) analyses comparing samples printed (a–c) without support and (d–f) with the support. (a) Cross-sectional XCT image showing cracks in sample without support. (b) Back-forward and (c) bottom-up projection views showing abundant continuous cracks. (d) Cross-sectional XCT image and (e) Back-forward projection view showing crack free region in samples with support. (f) Bottom-up view showing cracks initiated from support/built plate interfaces. Inserts on the upper right corner of each figure demonstrate the field of view with a red rectangle in relation to the whole specimen geometry. (For interpretation of the references to colour in this figure legend, the reader is referred to the Web version of this article.)

cracking mechanism present in this $Al_{92}Ti_2Fe_2Co_2Ni_2$ alloy appears different from prior studies. First, micron-size "cups and cones" morphology (Fig. 6g) implies that fracture happens in the solid state while both solidification cracking and liquation cracking necessitate the existence of thin liquid films. The ductile Al matrix is expected to deform while rigid intermetallic rosettes accommodate less strain. Fracture comes into rise after plastic Al dimples and disunites. These pointed, cellular flakes entail plasticity carried by dislocation motions in crystalline solids. However, liquation features either globular and dendritic surfaces in solidification cracking, or smooth and flat surfaces in liquation cracking, because cracking happens in the semi-solid state and liquid surface tension will prevent any singularity on the crack surface, as reported in AA2024 [52], AA7075 [2] and Al–Cu [26]. Additionally, liquidous cracks are typically manifested on the longitudinal centerline for solidification cracking or partially melted zone for liquation cracking. These fractographic traits differ from the predominant transversal cracking observed in this alloy.

Second, liquation is characteristic of micro-segregation of soluble elements near grain boundaries, like Mg, Cu, Zn [2]. The concentration of low-melting-point elements enlarges the solidification temperature range at the final stage. But in the case of $Al_{92}Ti_2Fe_2Co_2Ni_2$ alloy, these transition metals form precipitates primarily in the beginning and have limited solubility in Al at the eutectic point. Therefore, the limited amount and lifespan of liquidous films have minimal impact on cracking. In theory, according to the liquid backfill model [22] to predict liquidation susceptibility, the flat end of the $Al_{92}Ti_2Fe_2Co_2Ni_2$ solidification curve has a lower slope, $(dT/d(\sqrt{f_s}) < 100$ K, than the AA7075 (4579 K) and AlSi10Mg curves (645 K), which indicates lower cracking susceptibility. In fact, this criterion empirically considers the range where the solid fraction f_s is near a critical value around 1.0, as liquid backfill is most challenging at the final stage due to the considerable obstruction from the developed dendrites and the least amount of liquid. Thus, the slope (1111 K) derived conservatively from the broad range $[0.5 < f_s < 1.0]$ for this alloy may exaggerate the physical cracking susceptibility. Additional crack resistance could come from the nucleants breaking down columnar grains into equiaxed grains that better accommodate solidification strain [36]. Despite a low predicted cracking susceptibility based on the Scheil-Gulliver model, this alloy is still subject to severe cracking as described earlier.

Solid state cracking mechanisms that are less frequently considered in AM Al alloys include ductility dip cracking and strain-age cracking (reheat cracking) [14,16]. Ductility dip cracking refers to intergranular tearing in an intermediate temperature range where a material's ductility reaches a minimum. Strain-age cracking occurs when precipitation induces residual stress during post-weld heat treatment. Both terms are frequently discussed in the context of Ni-based superalloys or steels. These concepts may have insignificant effect on understanding cracking observed in the current custom-designed Al alloy.

Despite the elusive underlying mechanisms, it can be concluded from multiple observations that hot cracking is governed by residual stress for the customized $Al_{92}Ti_2Fe_2Co_2Ni_2$ alloy. First, the direct evidence comes from the significant tensile residual stress on the bottom interface in both directions (Fig. 10e and f). The magnitudes of tensile stress (0.5–1 GPa) may be somewhat exaggerated, but large tensile stress could tear apart specimens to release local stress concentrations. More frequent cracking normal to the longitudinal direction was observed, consistent with a lower σ_L, whereas a considerably larger σ_T in the transverse direction is retained without relaxation. In addition, the radial crack network resembling the delta at the crack tip (Fig. 6f) suggests residual stress relaxation can stop crack propagation, confirming the primary role of residual stress on cracking.

Second, single laser tracks experiments with various printing parameters are not subject to any cracking issue, in contrast to cracking in the bulk parts (seen as aggregates of laser tracks). This observation

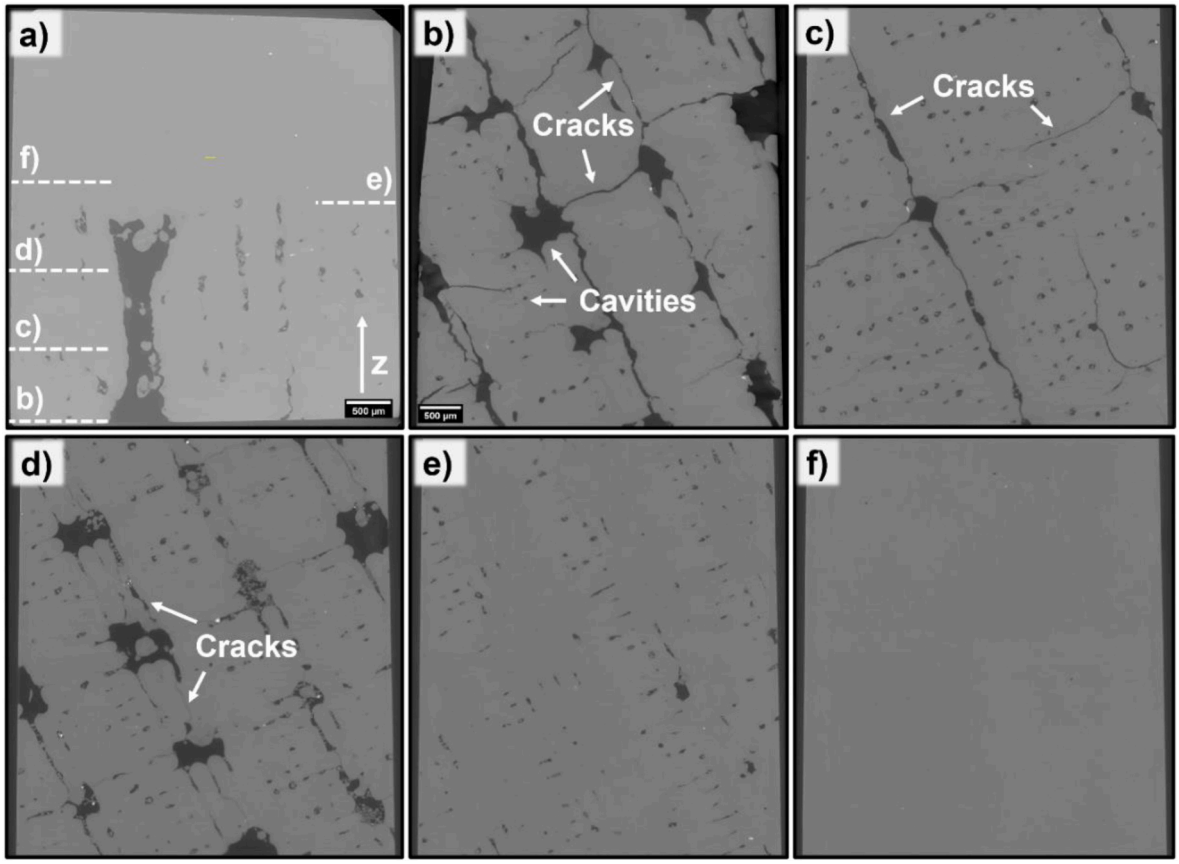

Fig. 14. (a) Vertical cross-section of the specimen printed on the support structure. (d–f) Series of horizontal sections in the building direction with the corresponding heights denoted in (a). Cracks were observed at plane b (h = 0.2 mm), c (h = 0.9 mm) and d (h = 2.0 mm) within support. (e) At the interface (h = 2.8 mm) between the support and the part, cracks significantly diminish. (f) Crack-free (h = 3.1 mm) solid building materials.

suggests that the development of cracking requires interactions of laser tracks and accumulation of residual stresses. It is well accepted that residual stress can accumulate from repeated thermal cycles during AM [61,62]. An over-simplified model states that during solidification of a single laser track, a fusion zone starts to consolidate and contract under the restraint of the surrounding materials, which would impose a tensile residual stress on the scanned region and a compressive residual stress near the heat affected zone [63]. For a general AM process that involves the printing of multiple layers, the established residual stress on the previous layer would be compensated, neutralized, or exacerbated by newly developed residual stress on the succeeding layer, and thus the evolution of residual stresses depends on the consolidation chronology and strategies. These interactions complicate the residual stress distribution and even lead to contradictory parametric effects on stress evolution [62]. In the case of AlSi10Mg, a tensile residual stress appeared on the bottom and a compressive stress appeared on the top as measured by the hole drilling strain gauge method [64], whereas in the case of 316 L stainless steel, an outer hull with tensile stress and a core with compressive stress was found utilizing neutron diffraction [63,65]. In spite of the divergence of residual stress evolution in AM metallic materials, both scenarios indicate that a tensile residual stress could couple with vulnerable defects to foster the upward crack propagation as shown from the side view of AM Al alloys (Fig. 6b).

Additionally, the observed crack healing effect driven by higher VEDs, contrary to literature reports [50,52], can be attributed to residual stress relaxation mechanism. A broader fusion zone (Fig. S2) resulting from increased energy input facilitates dislocation activities, extends the plastic deformability of alloys and also reduce residual stress by slowing down solidification. This improved plasticity is favorable for residual stress relaxation, resembling effects of a higher substrate temperature on crack mitigation [48–50].

4.3. The effects of support structure

Support structures are typically designed to support overhanging planes or facilitate sample removability from the build plate [66,67]. Here we adapted support structures for stress relief. The crack elimination effect of a support structure is validated for this custom high-strength $Al_{92}Ti_2Fe_2Co_2Ni_2$ alloy. Literature reports also find support could improve the relative density of materials in some cases [51,68,69]. As is observed from the distorted islands, the support structure enables flexibility and serves as a buffering layer between the rigid build plate and actual parts. It is believed that the crack mitigation effect stems primarily from this sacrificial compliance accomplished by this lattice design. Cracks are deliberately provoked in the support in a controllable fashion and residual stress gradually fades out. The support cushions the build parts of interest under cyclic thermal loading due to thermal shocks. Additionally, cavities could alleviate cracking by accommodating volume shrinkage and contraction during solidification. It is worth mentioning that our support structure differs from the common context in that our support structure has adjacent platelets that are partially merged as a consequence of a small spacing of 0.2 mm apart (density ~ 0.6), instead of being further separated, like 0.9 mm in this case [51]. This small spacing in a compact support seems to be critical, since more open structures with higher flexibility, like 0.4 mm for Support B (density ~ 0.3) in Fig. 11 and 1 mm for Support C (density ~ 0.06) in Fig. 11g–i, led to warpage and failure. Compared with solid dense bases, inter-platelet cavities are distributed in a speckled manner, which could uniformly alleviate geometric variance during solidification. Another effect of these open arrays in the support structure is to

toughen the support material by rounding crack tips. When intersecting with cracks, globular pores with smaller curvature can sustain high residual stress compared with sharp crack tips. Thus, pores could serve as crack sinks, and an improved cracking resistance is anticipated. In addition, supports lift parts above the surface on the build plate, where the printability is deteriorated by an abrupt change of cross section area for thermal exchange, fusion and diffusion in dissimilar materials joints across the interface. Beneficial to release residual stress, a higher temperature than the build plate temperature could be achieved by the bottlenecked heat dissipation through the open support structure, as unsintered powders and cavities between support platelets retard heat conduction. However, more importance should be attached to a balance between rigidness and compliance as well as crack sink effects, because other support designs with less heat exchange area and more prominent heat retention, like Support B and Support C, failed printing due to the significant warpage induced by the residual stress (Fig. 11d–i).

Despite the elaborated beneficial effects of this customized support structure, one may envision these influences decay quickly as printing moves away from the support-part interface. However, the experimental results suggest such crack-elimination effect could be largely preserved for printed alloys with large thickness or dimensions. As demonstrated in Fig. 14 with micro-CT crack rendering, cracks are absent for the printed parts above the 3-mm-thick support. Furthermore, crack-free 35 mm tall sheets and cylinders were vertically printed successfully with the aid of the support (Fig. 11c). These findings imply that cracking has a prominent dependency on history. In the case of direct printing on the substrate (without support), cracks nucleated on the initial layers due to residual stress can progress continuously through the successive layers, leading to long through-thickness cracks. Appropriate support structure is crucial in that it cuts off the initial nucleation of cracking, prohibiting the cracking formation. The current crack mitigation strategy may be widely applicable to manufacturing a suite of high strength AM alloys that are susceptible to cracking.

5. Conclusion

Hot cracking has been widely observed in high-strength Al alloys during additive manufacturing. This study presents numerous strategies that deal with hot cracking in a custom-designed high-strength $Al_{92}Ti_2Fe_2Co_2Ni_2$ alloy produced by LPBF. Printing parameter optimization on laser power and scanning speed found that a compromise had to be made between cracking and porosity. Further tuning of other AM parameters (defocus, contours, laser strip length, and scan strategy) demonstrates that cracking can be mitigated but not fully eliminated. More significantly, we found that the incorporation of a compliant support structure successfully eliminated all cracks as confirmed by micro-CT analyses. XRD analyses, fractography, and solidification history suggest that cracking is attributed to solid state tearing under substantial tensile residual stresses. The support structure releases residual stress and cushions the parts of interest under cyclic thermal impacts, thus eliminating cracks effectively. This study suggests that the proper design of support structures may have widespread applications to improve printability of various hard-to-print metallic materials that suffer from residual stresses.

CRediT authorship contribution statement

Anyu Shang: Conceptualization, Methodology, Formal analysis, Investigation, Data curation, Visualisation, Writing – original draft, Writing – review & editing. **Benjamin Stegman:** Formal analysis, Investigation, Data curation. **Daniel Sinclair:** Formal analysis, Investigation, Data curation, Writing – original draft, Writing – review & editing. **Xuanyu Sheng:** Data curation, Visualization. **Luke Hoppenrath:** Data curation, Visualization. **Chao Shen:** Data curation, Visualization. **Ke Xu:** Data curation, Visualization. **Emiliano Flores:** Data curation. **Haiyan Wang:** Funding acquisition, Resources, Supervision. **Nikhilesh Chawla:** Resources, Supervision, Software, Writing – review & editing. **Xinghang Zhang:** Conceptualization, Project administration, Resources, Supervision, Validation, Writing – review & editing.

Declaration of competing interest

The authors declare the following financial interests/personal relationships which may be considered as potential competing interests: Anyu Shang, Ben Stegman, Xinghang Zhang, Haiyan Wang has a patent pending to US Patent Office. If there are other authors, they declare that they have no known competing financial interests or personal relationships that could have appeared to influence the work reported in this paper.

Acknowledgements

This work is supported primarily by NSF-DMR-MMN 2210152. Access to the Electron Microscopy Facility center at Purdue University is also acknowledged. B. S. and H.W. acknowledge the support by the U.S. Office of Naval Research (Contract No N00014-22-1-2160). D.S. and N. C. acknowledge support from the U.S. Office of Naval Research (Contract # is N00014-20-1-2865) as well as the National Science Foundation Graduate Research Fellowship Program (NSF GRFP DGE-1842166). The authors also want to acknowledge the assistance on the sample preparation from Jack Lopez, Chenglu Tang, Bohua Peter Zhang, Jialong Huang, and valuable insights in cracking mechanisms from an anonymous reviewer.

Appendix A. Supplementary data

Supplementary data to this article can be found online at https://doi.org/10.1016/j.jmrt.2024.04.191.

References

[1] Mehta A, Zhou L, Huynh T, Park S, Hyer H, Song S, et al. Additive manufacturing and mechanical properties of the dense and crack free Zr-modified aluminum alloy 6061 fabricated by the laser-powder bed fusion. Addit Manuf 2021;41:101966. https://doi.org/10.1016/j.addma.2021.101966.

[2] Stopyra W, Gruber K, Smolina I, Kurzynowski T, Kuźnicka B. Laser powder bed fusion of AA7075 alloy: influence of process parameters on porosity and hot cracking. Addit Manuf 2020;35:101270. https://doi.org/10.1016/j.addma.2020.101270.

[3] Galy C, Le Guen E, Lacoste E, Arvieu C. Main defects observed in aluminum alloy parts produced by SLM: from causes to consequences. Addit Manuf 2018;22:165–75. https://doi.org/10.1016/j.addma.2018.05.005.

[4] Aboulkhair NT. 3D printing of Aluminium alloys_ Additive Manufacturing of Aluminium alloys using selective laser melting. Prog Mater Sci 2019;45.

[5] Kotadia HR, Gibbons G, Das A, Howes PD. A review of laser powder bed fusion additive manufacturing of aluminium alloys: microstructure and properties. Addit Manuf 2021;46:102155. https://doi.org/10.1016/j.addma.2021.102155.

[6] Zhao L, Song L, Santos Macías JG, Zhu Y, Huang M, Simar A, et al. Review on the correlation between microstructure and mechanical performance for laser powder bed fusion AlSi10Mg. Addit Manuf 2022;56:102914. https://doi.org/10.1016/j.addma.2022.102914.

[7] Kusoglu IM, Gökce B, Barcikowski S. Research trends in laser powder bed fusion of Al alloys within the last decade. Addit Manuf 2020;36:101489. https://doi.org/10.1016/j.addma.2020.101489.

[8] Hyer H, Zhou L, Mehta A, Park S, Huynh T, Song S, et al. Composition-dependent solidification cracking of aluminum-silicon alloys during laser powder bed fusion. Acta Mater 2021;208:116698. https://doi.org/10.1016/j.actamat.2021.116698.

[9] Aboulkhair NT, Everitt NM, Ashcroft I, Tuck C. Reducing porosity in AlSi10Mg parts processed by selective laser melting. Addit Manuf 2014;1–4:77–86. https://doi.org/10.1016/j.addma.2014.08.001.

[10] Aboulkhair NT, Maskery I, Tuck C, Ashcroft I, Everitt NM. Improving the fatigue behaviour of a selectively laser melted aluminium alloy: influence of heat treatment and surface quality. Mater Des 2016;104:174–82. https://doi.org/10.1016/j.matdes.2016.05.041.

[11] Maamoun AH, Elbestawi M, Dosbaeva GK, Veldhuis SC. Thermal post-processing of AlSi10Mg parts produced by Selective Laser Melting using recycled powder. Addit Manuf 2018;21:234–47. https://doi.org/10.1016/j.addma.2018.03.014.

[12] Miao K, Zhou H, Gao Y, Deng X, Lu Z, Li D. Laser powder-bed-fusion of Si3N4 reinforced AlSi10Mg composites: processing, mechanical properties and strengthening mechanisms. Mater Sci Eng, A 2021;825:141874. https://doi.org/10.1016/j.msea.2021.141874.

[13] Li XP, Ji G, Chen Z, Addad A, Wu Y, Wang HW, et al. Selective laser melting of nano-TiB2 decorated AlSi10Mg alloy with high fracture strength and ductility. Acta Mater 2017;129:183–93. https://doi.org/10.1016/j.actamat.2017.02.062.
[14] Kou S. Solidification and liquation cracking issues in welding. 2003.
[15] Chauvet E, Kontis P, Jägle EA, Gault B, Raabe D, Tassin C, et al. Hot cracking mechanism affecting a non-weldable Ni-based superalloy produced by selective electron Beam Melting. Acta Mater 2018;142:82–94. https://doi.org/10.1016/j.actamat.2017.09.047.
[16] Welding metallurgy and weldability of nickel-base alloys. first ed. John Wiley & Sons, Ltd; 2009. https://doi.org/10.1002/9780470500262.
[17] Li S, Apelian D. Hot tearing of aluminum alloys: a critical literature review. Inter Metalcast 2011;5:23–40. https://doi.org/10.1007/BF03355505.
[18] Eskin DG, Suyitno Katgerman L. Mechanical properties in the semi-solid state and hot tearing of aluminium alloys. Prog Mater Sci 2004;49:629–711. https://doi.org/10.1016/S0079-6425(03)00037-9.
[19] Li Y, Li H, Katgerman L, Du Q, Zhang J, Zhuang L. Recent advances in hot tearing during casting of aluminium alloys. Prog Mater Sci 2021;117:100741. https://doi.org/10.1016/j.pmatsci.2020.100741.
[20] Ghaini FM, Sheikhi M, Torkamany MJ, Sabbaghzadeh J. The relation between liquation and solidification cracks in pulsed laser welding of 2024 aluminium alloy. Mater Sci Eng, A 2009;519:167–71. https://doi.org/10.1016/j.msea.2009.04.056.
[21] Rappaz M, Drezet J-M, Gremaud M. A new hot-tearing criterion. Metall Mater Trans A 1999;30:449–55. https://doi.org/10.1007/s11661-999-0334-z.
[22] Kou S. A criterion for cracking during solidification. Acta Mater 2015;88:366–74. https://doi.org/10.1016/j.actamat.2015.01.034.
[23] Eskin DG, Katgerman LSuyitno, Mooney JF. Contraction of aluminum alloys during and after solidification. Metall Mater Trans A 2004;35:1325–35. https://doi.org/10.1007/s11661-004-0307-1.
[24] Li Y, Gu D. Parametric analysis of thermal behavior during selective laser melting additive manufacturing of aluminum alloy powder. Mater Des 2014;63:856–67. https://doi.org/10.1016/j.matdes.2014.07.006.
[25] Pauly S, Wang P, Kühn U, Kosiba K. Experimental determination of cooling rates in selectively laser-melted eutectic Al-33Cu. Addit Manuf 2018;22:753–7. https://doi.org/10.1016/j.addma.2018.05.034.
[26] Hu Z, Nie X, Qi Y, Zhang H, Zhu H. Cracking criterion for high strength Al–Cu alloys fabricated by selective laser melting. Addit Manuf 2021;37:101709. https://doi.org/10.1016/j.addma.2020.101709.
[27] Xinwei L, Shi S, Shuang H, Xiaogang H, Qiang Z, Hongxing L, et al. Microstructure, solidification behavior and mechanical properties of Al-Si-Mg-Ti/TiC fabricated by selective laser melting. Addit Manuf 2020;34:101326. https://doi.org/10.1016/j.addma.2020.101326.
[28] Zheng T, Pan S, Murali N, Li B, Li X. Selective laser melting of novel 7075 aluminum powders with internally dispersed TiC nanoparticles. Mater Lett 2022;319:132268. https://doi.org/10.1016/j.matlet.2022.132268.
[29] Lin T-C, Cao C, Sokoluk M, Jiang L, Wang X, Schoenung JM, et al. Aluminum with dispersed nanoparticles by laser additive manufacturing. Nat Commun 2019;10:4124. https://doi.org/10.1038/s41467-019-12047-2.
[30] Zhou SY, Su Y, Wang H, Enz J, Ebel T, Yan M. Selective laser melting additive manufacturing of 7xxx series Al-Zn-Mg-Cu alloy: cracking elimination by co-incorporation of Si and TiB2. Addit Manuf 2020;36:101458. https://doi.org/10.1016/j.addma.2020.101458.
[31] Tan Q, Zhang J, Sun Q, Fan Z, Li G, Yin Y, et al. Inoculation treatment of an additively manufactured 2024 aluminium alloy with titanium nanoparticles. Acta Mater 2020;196:1–16. https://doi.org/10.1016/j.actamat.2020.06.026.
[32] Mair P, Braun J, Kaserer L, March L, Schimbäck D, Letofsky-Papst I, et al. Unique microstructure evolution of a novel Ti-modified Al-Cu alloy processed using laser powder bed fusion. Mater Today Commun 2022;31:103353. https://doi.org/10.1016/j.mtcomm.2022.103353.
[33] Tan Q, Fan Z, Tang X, Yin Y, Li G, Huang D, et al. A novel strategy to additively manufacture 7075 aluminium alloy with selective laser melting. Mater Sci Eng, A 2021;821:141638. https://doi.org/10.1016/j.msea.2021.141638.
[34] Nie X, Zhang H, Zhu H, Hu Z, Ke L, Zeng X. Effect of Zr content on formability, microstructure and mechanical properties of selective laser melted Zr modified Al-4.24Cu-1.97Mg-0.56Mn alloys. J Alloys Compd 2018;764:977–86. https://doi.org/10.1016/j.jallcom.2018.06.032.
[35] Zhang H, Zhu H, Nie X, Yin J, Hu Z, Zeng X. Effect of Zirconium addition on crack, microstructure and mechanical behavior of selective laser melted Al-Cu-Mg alloy. Scripta Mater 2017;134:6–10. https://doi.org/10.1016/j.scriptamat.2017.02.036.
[36] Martin JH, Yahata BD, Hundley JM, Mayer JA, Schaedler TA, Pollock TM. 3D printing of high-strength aluminium alloys. Nature 2017;549:365–9. https://doi.org/10.1038/nature23894.
[37] Geng Y, Jia C, Xu J, Zhang Z, Ju H, Wang D, et al. Selective laser melting of a novel high-strength Er- and Zr-modified Al-Mn-Mg alloy. Mater Lett 2022;313:131762. https://doi.org/10.1016/j.matlet.2022.131762.
[38] Tang H, Geng Y, Bian S, Xu J, Zhang Z. An ultra-high strength over 700 MPa in Al-Mn-Mg-Sc-Zr alloy fabricated by selective laser melting. Acta Metall Sin 2022;35:466–74. https://doi.org/10.1007/s40195-021-01286-2.
[39] Zhang H, Gu D, Yang J, Dai D, Zhao T, Hong C, et al. Selective laser melting of rare earth element Sc modified aluminum alloy: thermodynamics of precipitation behavior and its influence on mechanical properties. Addit Manuf 2018;23:1–12. https://doi.org/10.1016/j.addma.2018.07.002.
[40] Spierings AB, Dawson K, Voegtlin M, Palm F, Uggowitzer PJ. Microstructure and mechanical properties of as-processed scandium-modified aluminium using selective laser melting. CIRP Annals 2016;65:213–6. https://doi.org/10.1016/j.cirp.2016.04.057.
[41] Schmidtke K, Palm F, Hawkins A, Emmelmann C. Process and mechanical properties: applicability of a scandium modified Al-alloy for laser additive manufacturing. Phys Procedia 2011;12:369–74. https://doi.org/10.1016/j.phpro.2011.03.047.
[42] Li R, Wang M, Li Z, Cao P, Yuan T, Zhu H. Developing a high-strength Al-Mg-Si-Sc-Zr alloy for selective laser melting: crack-inhibiting and multiple strengthening mechanisms. Acta Mater 2020;193:83–98. https://doi.org/10.1016/j.actamat.2020.03.060.
[43] Bayoumy D, Schliephake D, Dietrich S, Wu XH, Zhu YM, Huang AJ. Intensive processing optimization for achieving strong and ductile Al-Mn-Mg-Sc-Zr alloy produced by selective laser melting. Mater Des 2021;198:109317. https://doi.org/10.1016/j.matdes.2020.109317.
[44] Plotkowski A, Sisco K, Bahl S, Shyam A, Yang Y, Allard L, et al. Microstructure and properties of a high temperature Al–Ce–Mn alloy produced by additive manufacturing. Acta Mater 2020;196:595–608. https://doi.org/10.1016/j.actamat.2020.07.014.
[45] Sisco K, Plotkowski A, Yang Y, Leonard D, Stump B, Nandwana P, et al. Microstructure and properties of additively manufactured Al–Ce–Mg alloys. Sci Rep 2021;11:6953. https://doi.org/10.1038/s41598-021-86370-4.
[46] Qi T, Zhu H, Zhang H, Yin J, Ke L, Zeng X. Selective laser melting of Al7050 powder: melting mode transition and comparison of the characteristics between the keyhole and conduction mode. Mater Des 2017;135:257–66. https://doi.org/10.1016/j.matdes.2017.09.014.
[47] Tan Q, Liu Y, Fan Z, Zhang J, Yin Y, Zhang M-X. Effect of processing parameters on the densification of an additively manufactured 2024 Al alloy. J Mater Sci Technol 2020;58:34–45. https://doi.org/10.1016/j.jmst.2020.03.070.
[48] Mertens R, Dadbakhsh S, Humbeeck JV, Kruth J-P. Application of base plate preheating during selective laser melting. Procedia CIRP 2018;74:5–11. https://doi.org/10.1016/j.procir.2018.08.002.
[49] Uddin SZ, Murr LE, Terrazas CA, Morton P, Roberson DA, Wicker RB. Processing and characterization of crack-free aluminum 6061 using high-temperature heating in laser powder bed fusion additive manufacturing. Addit Manuf 2018;22:405–15. https://doi.org/10.1016/j.addma.2018.05.047.
[50] Kaufmann N, Imran M, Wischeropp TM, Emmelmann C, Siddique S, Walther F. Influence of process parameters on the quality of aluminium alloy EN AW 7075 using selective laser melting (SLM). Phys Procedia 2016;83:918–26. https://doi.org/10.1016/j.phpro.2016.08.096.
[51] Koutny D, Palousek D, Pantelejev L, Hoeller C, Pichler R, Tesicky L, et al. Influence of scanning strategies on processing of aluminum alloy EN AW 2618 using selective laser melting. Materials 2018;11:298. https://doi.org/10.3390/ma11020298.
[52] Cao Y, Wei HL, Yang T, Liu TT, Liao WH. Printability assessment with porosity and solidification cracking susceptibilities for a high strength aluminum alloy during laser powder bed fusion. Addit Manuf 2021;46:102103. https://doi.org/10.1016/j.addma.2021.102103.
[53] Schindelin J, Arganda-Carreras I, Frise E, Kaynig V, Longair M, Pietzsch T, et al. Fiji: an open-source platform for biological-image analysis. Nat Methods 2012;9:676–82. https://doi.org/10.1038/nmeth.2019.
[54] Arganda-Carreras I, Fernández-González R, Muñoz-Barrutia A, Ortiz-De-Solorzano C. 3D reconstruction of histological sections: application to mammary gland tissue. Microsc Res Tech 2010;73:1019–29. https://doi.org/10.1002/jemt.20829.
[55] Wagner T, Hiner M, xraynaud. thorstenwagner/ij-ridgedetection: Ridge Detection 1.4.0 2017. https://doi.org/10.5281/zenodo.845874.
[56] Prevey PS, Research L. X-ray diffraction residual stress techniques n.d.:vol. 18.
[57] Yadroitsev I, Smurov I. Selective laser melting technology: from the single laser melted track stability to 3D parts of complex shape. Phys Procedia 2010;5:551–60. https://doi.org/10.1016/j.phpro.2010.08.083.
[58] Di W, Yongqiang Y, Xubin S, Yonghua C. Study on energy input and its influences on single-track,multi-track, and multi-layer in SLM. Int J Adv Manuf Technol 2012;58:1189–99. https://doi.org/10.1007/s00170-011-3443-y.
[59] Zhou S, Su Y, Gu R, Wang Z, Zhou Y, Ma Q, et al. Impacts of defocusing amount and molten pool boundaries on mechanical properties and microstructure of selective laser melted AlSi10Mg. Materials 2018;12:73. https://doi.org/10.3390/ma12010073.
[60] Chen Y, Zhang K, Huang J, Hosseini SRE, Li Z. Characterization of heat affected zone liquation cracking in laser additive manufacturing of Inconel 718. Mater Des 2016;90:586–94. https://doi.org/10.1016/j.matdes.2015.10.155.
[61] Zhao L, Santos Macías JG, Dolimont A, Simar A, Rivière-Lorphèvre E. Comparison of residual stresses obtained by the crack compliance method for parts produced by different metal additive manufacturing techniques and after friction stir processing. Addit Manuf 2020;36:101499. https://doi.org/10.1016/j.addma.2020.101499.
[62] Xiao Z, Chen C, Zhu H, Hu Z, Nagarajan B, Guo L, et al. Study of residual stress in selective laser melting of Ti6Al4V. Mater Des 2020;193:108846. https://doi.org/10.1016/j.matdes.2020.108846.
[63] Li C, Liu ZY, Fang XY, Guo YB. Residual stress in metal additive manufacturing. Procedia CIRP 2018;71:348–53. https://doi.org/10.1016/j.procir.2018.05.039.
[64] Salmi A, Atzeni E, Iuliano L, Galati M. Experimental analysis of residual stresses on AlSi10Mg parts produced by means of selective laser melting (SLM). Procedia CIRP 2017;62:458–63. https://doi.org/10.1016/j.procir.2016.06.030.
[65] Wu AS, Brown DW, Kumar M, Gallegos GF, King WE. An experimental investigation into additive manufacturing-induced residual stresses in 316L stainless steel. Metall Mater Trans A 2014;45:6260–70. https://doi.org/10.1007/s11661-014-2549-x.

[66] Hussein A, Hao L, Yan C, Everson R, Young P. Advanced lattice support structures for metal additive manufacturing. J Mater Process Technol 2013;213:1019–26. https://doi.org/10.1016/j.jmatprotec.2013.01.020.
[67] Järvinen J-P, Matilainen V, Li X, Piili H, Salminen A, Mäkelä I, et al. Characterization of effect of support structures in laser additive manufacturing of stainless steel. Phys Procedia 2014;56:72–81. https://doi.org/10.1016/j.phpro.2014.08.099.
[68] Ahuja B, Karg M, Nagulin KYu, Schmidt M. Fabrication and characterization of high strength Al-Cu alloys processed using laser beam melting in metal powder bed. Phys Procedia 2014;56:135–46. https://doi.org/10.1016/j.phpro.2014.08.156.
[69] Wang D, Yu C, Ma J, Liu W, Shen Z. Densification and crack suppression in selective laser melting of pure molybdenum. Mater Des 2017;129:44–52. https://doi.org/10.1016/j.matdes.2017.04.094.